NANO LETTERS

Letter

Cite This: Nano Lett. XXXX, XXX, XXX−XXX

pubs.acs.org/NanoLett

# Quantitative Imaging of Organic Ligand Density on Anisotropic Inorganic Nanocrystals

Blanka E. Janicek,[†] Joshua G. Hinman,[‡] Jordan J. Hinman,[‡] Sang hyun Bae,[†] Meng Wu,[‡] Jacob Turner,[‡] Huei-Huei Chang,[‡] Eugene Park,[†] Rachel Lawless,[†] Kenneth S. Suslick,[‡] Catherine J. Murphy,[‡,§] and Pinshane Y. Huang*[,†,§]

[†]Department of Materials Science and Engineering, University of Illinois at Urbana−Champaign, Urbana, Illinois 61801, United States

[‡]Department of Chemistry, University of Illinois at Urbana−Champaign, Urbana, Illinois 61801, United States

[§]Materials Research Laboratory, University of Illinois at Urbana−Champaign, Urbana, Illinois 61801, United States

Supporting Information

**ABSTRACT:** A longstanding challenge in nanoparticle characterization is to understand anisotropic distributions of organic ligands at the surface of inorganic nanoparticles. Here, we show that using electron energy loss spectroscopy in an aberration-corrected scanning transmission electron microscope we can directly visualize and quantify ligand distributions on gold nanorods (AuNRs). These experiments analyze dozens of particles on graphene substrates, providing insight into how ligand binding densities vary within and between individual nanoparticles. We demonstrate that the distribution of cetyltrimethylammonium bromide (CTAB) on AuNRs is anisotropic, with a 30% decrease in ligand density at the poles of the nanoparticles. In contrast, the distribution of (16-mercaptohexadecyl)trimethylammonium bromide (MTAB) is more uniform. These results are consistent with literature reported higher reactivity at the ends of CTAB-coated AuNRs. Our results demonstrate the impact of electron spectroscopy to probe molecular distributions at soft−hard interfaces and how they produce spatially heterogeneous properties in colloidal nanoparticles.

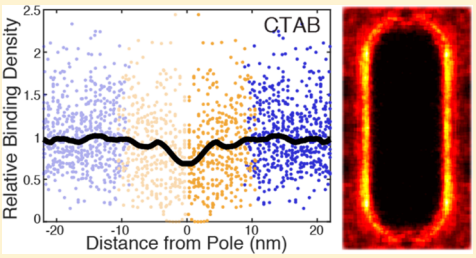


**KEYWORDS:** *ligand characterization, ligand binding density, gold nanorods, cetyltrimethylammonium bromide, electron energy loss spectroscopy, scanning transmission electron microscopy*

Anisotropic nanomaterials offer the potential for profound control over chemical and physical properties on the nanoscale. Nanoparticles with controlled shape anisotropies such as rods, polyhedra, and branched structures exhibit tailored plasmonic response and catalytic reactivity.[1] Nanoparticles with chemical anisotropy can undergo site-specific chemical reactions and self-assemble into complex 3D supramolecular structures.[2−4] Across these systems, organic molecules play a key role in producing anisotropy by modifying the nanoscale kinetic growth pathways, chemical reactivity, and interparticle interaction potentials of inorganic nanoparticles.[3,5] For example, local variations in ligand density are thought to play an essential role in the synthesis of complex and anisotropic nanoparticles.[1,2,5−8] Patchiness in the organic ligand density on inorganic nanocrystals has been invoked in numerous functional properties of these materials, ranging from plasmonic coupling to cellular uptake.[4,9] In self-assembled nanoparticle superlattices, anisotropic ligand distributions allow independent control of nanoparticle "atoms" and the orientation of their ligand "bonds."[3,10] In these areas, an ultimate goal is to be able to understand, manipulate, and design this molecular coating to guide the synthesis and assembly of nanostructures with tailored properties.

To understand these processes, a nanoscale understanding of the local binding density of organic molecules at soft−hard interfaces is paramount. While quantifying the distributions of organics on soft−hard interfaces is of critical importance, it remains a substantial challenge to characterize such interfaces at the nanoscale. For example, in transmission electron microscopy (TEM), the elastic scattering signal from surface-bound organic ligands is two orders of magnitude smaller than that from a gold nanocrystal. Organic molecules are also readily damaged by the electron beam, making them difficult to probe at high-resolution. Moreover, while high-resolution methods such as TEM and scanning tunneling microscopy typically contain measurements of just a few particles, nanoparticles can be highly heterogeneous in their structure and chemistry. In comparison, bulk characterization methods such as small-angle X-ray scattering, UV−vis spectroscopy, and nuclear magnetic resonance (NMR) spectroscopy lack the spatial resolution to measure how molecular distributions vary within and between particles. Very few studies have probed the

**Received:** June 14, 2019
**Revised:** July 24, 2019
**Published:** August 19, 2019






DOI: 10.1021/acs.nanolett.9b02434
Nano Lett. XXXX, XXX, XXX−XXX

distributions of organic surface ligands at the nanoscale,[11−14] and none have been able to quantify nanoscale variations in ligand densities.

Here we demonstrate methods that directly image and quantify organic molecules at the soft−hard interface of gold nanorods (AuNRs). Well-established synthetic protocols provide control over the size, shape, and aspect ratio of AuNRs,[6,15,16] making them ideal for applications in plasmonics, biomedical diagnostics, and therapeutics.[1,17] AuNRs also serve as a model system for understanding structural and functional anisotropy in colloidal nanostructures.[5,18] We examine three systems of AuNRs: cetyltrimethylammonium bromide (CTAB)-coated AuNRs, (16-mercaptohexadecyl)-trimethylammonium bromide (MTAB)-coated mini AuNRs, and mesoporous silica-coated AuNRs. A defining characteristic of CTAB-coated AuNRs is that their growth kinetics and chemical reactivity are highly anisotropic. Indeed, CTAB-coated nanorods are one of the most studied anisotropic systems, where the spatial density of organic ligands are thought to induce structural and chemical anisotropy on the nanoscale. Acid etching,[19] thiol functionalization,[20] and deposition of mesoporous silica coatings[21,22] each appear to react initially at the ends of CTAB-coated AuNRs. These effects, as well as the growth and the postsynthetic end-to-end assembly of AuNRs, have been attributed to nanoscale anisotropy in the ligand distributions on the nanorod surface.[4,5,7,8] These properties point toward a reduced CTAB binding density on the ends of AuNRs, although recent work has disputed this assumption.[23] Theoretical predictions suggest that anisotropic ligand distributions arise from several factors including curvature,[24] localized variations in inorganic surface composition,[6,18] and facet-dependent binding densities.[7,8] These theories have been difficult to verify because of the lack of direct experimental methods to measure the local distribution of organic ligands on the nanoparticle surface.

In this work, we use electron energy loss spectroscopy in an aberration-corrected scanning transmission electron microscope (STEM-EELS) to visualize and quantify organic ligands on the surfaces of AuNRs. Figure 1 illustrates our approach, which focuses on a scalable method to deposit and study AuNRs on atomically thin graphene substrates. Figure 1a shows an annular dark-field (ADF) STEM image of a graphene support before deposition of AuNRs. In this image, individual carbon atoms are visible forming the honeycomb lattice of graphene. The benefits of the graphene substrate are 2-fold. First, the 1-atom thick (∼0.3 nm) graphene substrate provides an ultralow background,[25] maximizing the contrast from the organic layers in EELS spectral images. In contrast, conventional TEM substrates of 2−20 nm thick amorphous carbon produce large background signals that obscure scattering signals from organic molecules. Second, graphene substrates have also been shown to increase dose resistance of the supported materials by providing high electrical and thermal conductivity and by acting as a physical barrier to knock-on damage.[26] While exfoliated graphene flakes have demonstrated exceptional promise as TEM imaging substrates for studying soft−hard interfaces,[25] they offer extremely limited areas of single-layer graphene substrates, typically totaling 100 nm to a few microns per TEM grid. These limitations have confined previous studies of soft−hard nanoparticle interfaces on graphene to report data from just one or a few particles.[25] Instead, we prepare large-area, mm-scale single layer graphene substrates. Chemical vapor deposition (CVD) grown graphene

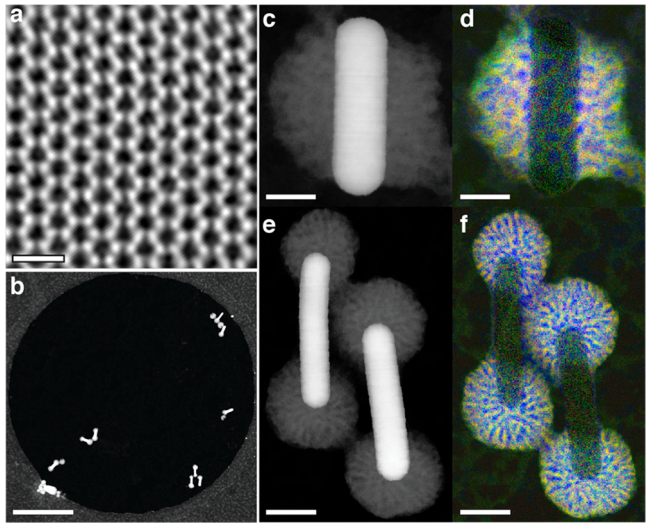


**Figure 1.** STEM-EELS imaging and composition mapping of mesoporous silica-coated AuNRs on graphene. (a) Aberration-corrected summed ADF-STEM image of clean, suspended graphene prior to deposition of particles. The image is a cross-correlated sum of six images. Scale bar is 0.5 nm. (b) Low-magnification ADF-STEM image showing several AuNRs after deposition onto suspended graphene via ultrasonic nebulization. Scale bar is 500 nm. (c,e) ADF-STEM images and (d,f) corresponding EELS compositional maps of AuNRs. Each nanorod is either (c,d) side-coated, scale bars are 15 nm, or (e,f) end-coated with mesoporous silica, scale bars are 30 nm. In the EELS maps (d,f), carbon is shown in blue and the mesoporous silica in yellow (using signal from Si and O). The EELS maps show the organic molecules are confined to the pores of the silica. In side-coated nanorods, we observe a pore distribution roughly parallel to the transverse axis with a 4 ± 1 (st. dev.) nm pore width. In contrast, the pore distribution in end-coated nanorods is radial with a 2.5 ± 0.5 (st. dev.) nm average width.

was transferred to a TEM grid using a polymer-based transfer followed by a series of cleaning steps (see Supporting Information (SI)). The resulting grids have monolayer graphene suspended over 2 $\mu$m holes, with approximately 70% of the holes covered across the entire 3 mm grid.[27]

Figure 1b shows a low-magnification ADF-STEM image of silica-coated AuNRs deposited on the graphene substrate. A challenge in using CVD graphene substrates for colloidal nanoparticles is how to deposit nanoparticles from solution without damaging the fragile 1-atom thick substrate. We used a recently published ultrasonication nebulization technique where ultrasound is used to produce a mist of micron-scale droplets that are deposited at low velocity onto the TEM grid.[27−29] This method deposits nanoparticles uniformly across the entire TEM grid while minimizing nanoparticle aggregation and avoiding rupturing the suspended graphene. As a final step, we bake the samples overnight in vacuum at 130 °C to remove the carrier liquid and minimize carbon contamination. This temperature is well below the ∼200 °C temperature at which MTAB and CTAB desorb from the gold surface.[30,31]

By conducting STEM-EELS on nanorods supported by graphene, we are able to achieve high detection sensitivity for organic ligands at the nanoscale. Figure 1c−f shows ADF-STEM images and EELS maps of AuNRs selectively coated on either the sides or ends with mesoporous silica. In these samples, CTAB is incorporated into the mesoporous silica during growth, templating the formation of pores.[21,22] As shown in Figure 1c,e, ADF-STEM offers limited utility for


DOI: 10.1021/acs.nanolett.9b02434
Nano Lett. XXXX, XXX, XXX−XXX

imaging the light elements because the image contrast scales as the atomic number $Z^{\gamma}$, where $1.3 < \gamma < 2$. Instead, we use EELS spectral imaging (Figure 1d,f), to produce 2D maps of the carbon (blue) and silicon and oxygen (yellow) distributions around AuNRs. While EELS is commonly used to map the composition of inorganic elements in nanoparticles,[32] it has only rarely been applied to map their organic molecular shells.[12] Figure 1d,f shows that EELS offers excellent contrast for organic molecules on graphene and can detect their nanoscale distribution, though we note that these experiments must be done with care to control for the potential impact of electron beam damage (see SI). Our measurements also show that the graphene grids provide an approximately 4× increase in signal-to-background ratio of the CTAB carbon signal on graphene over conventional ultrathin amorphous carbon substrates (see Figure S1). Together, the above methods substantially improve our sensitivity to organic molecules, allowing us to characterize organic ligand distribution at the soft−hard interface of AuNRs.

We apply these methods to study the distributions of CTAB and MTAB on AuNRs. CTAB-coated single-crystal AuNRs were synthesized using a single-step, silver-assisted, seeded growth method. CTAB-coated Au seeds were prepared and then added to a nanorod growth solution containing $HAuCl_4$ precursor, previously reduced by either hydroquinone or ascorbic acid, in the presence of excess of CTAB and trace silver nitrate.[6,15,33] MTAB-coated mini AuNRs were prepared using the same CTAB-coated seeds and added to the growth solution with the addition of HCl, followed by ligand exchange of CTAB with MTAB.[16,34] The average dimensions (length × width) of the CTAB-coated rods are 45 ± 5 (st. dev.) nm × 15 ± 2 (st. dev.) nm with an aspect ratio of 3.2. The MTAB-coated rods are 31 ± 5 (st. dev.) nm × 11 ± 1 (st. dev.) nm with an aspect ratio of 3.0.

Figure 2a−c shows an ADF-STEM image of two CTAB-coated AuNRs on graphene and corresponding carbon and nitrogen elemental maps acquired using EELS spectral imaging. In Figure 2b,c, C and N are present in an organic shell of 2.4 ± 0.3 nm, comparable to the 3.2−3.4 nm width of the CTAB shell previously observed in colloidal[35] and dried nanoparticles.[36] Importantly, the simultaneous presence of C and N indicates that the shell is composed of CTAB ($C_{19}H_{42}BrN$) rather than other organic residues. These data also demonstrate the ability of EELS to detect the functional groups of organic molecules, here the amine group of CTAB, in the STEM.

Major advantages of our sample preparation and EELS methods are that they achieve nanoscale spatial resolution, detect subtle changes in molecular distribution, and can be readily scaled to measure dozens of nanoparticles. Figure 2d−i shows EELS maps of the CTAB distribution (d−f) and the MTAB distribution (2g−i) around six different AuNRs. These data are a subset of the 32 particles we measured and analyzed in this work (see Figure S4). In these images, we observe large variations in the ligand distributions between particles and within individual particles; the MTAB coatings appear more uniform than the CTAB coatings. As shown in Figure 3, we use these carbon maps to quantify variations in the binding densities of organic ligands on the surface of individual nanorods. We use carbon as the indicator of the ligand density, rather than other elements such as N or S, because of its higher abundance and stability under the electron beam. Additionally, the graphene substrate provides a built-in standard to quantify

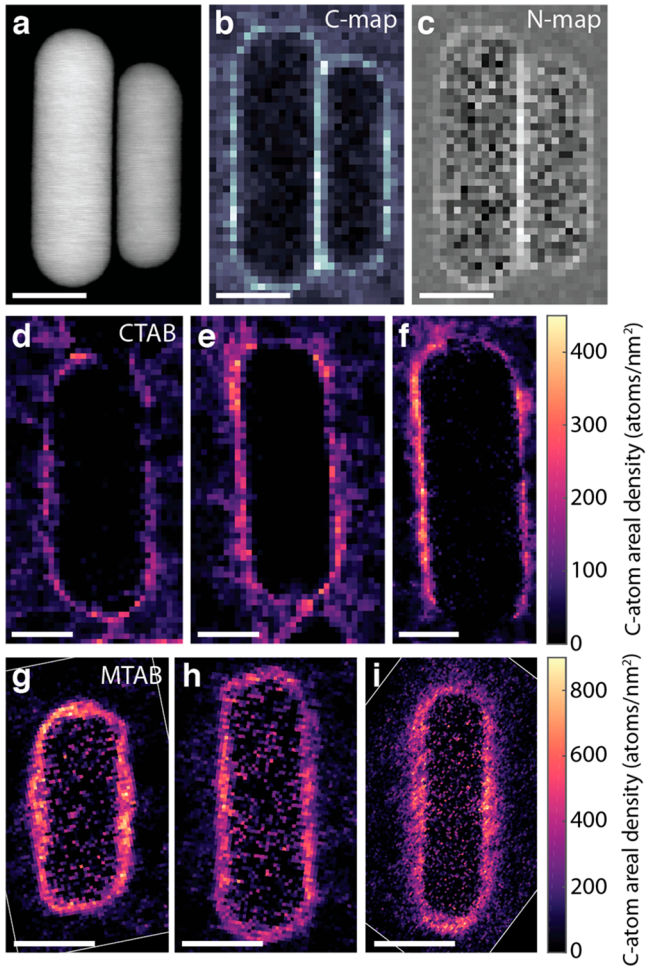


**Figure 2.** ADF-STEM and EELS spectral maps of ligand-coated AuNRs. (a) ADF-STEM image of two CTAB-coated AuNRs deposited on a graphene support. (b,c) EELS spectral maps of carbon (b) and nitrogen (c) from the same region as (a), obtained through background subtraction and integration of the C−K and N−K edges. These data show that a shell of 2.4 ± 0.3 nm width containing C and N surrounds the AuNRs. Multiple inelastic scattering from the gold makes it difficult to detect carbon that is overlapping the AuNR in projection; as a result, while the carbon density on the nanorod appears lower than on the graphene substrate in EELS maps such as in (b), this does not reflect a real decrease in carbon concentration. These effects do not impact our ligand measurements at the edges of the nanorods. CTAB contains one nitrogen per molecule, a C/N ratio of 19:1, resulting in the lowered signal-to-noise in the nitrogen map. (d−f) Three EELS carbon compositional maps of CTAB-coated AuNRs with the graphene background subtracted. The nanorod in (f) is isolated, while the nanorods in (d,e) are adjacent to nanorods touching one (e) or both (d) poles of the rod. The intensity scale bar indicates the local areal density (2D projected) of carbon atoms after subtraction of the graphene background. (g−i) Three EELS carbon compositional maps of MTAB-coated mini AuNRs again with the graphene background subtracted. All three rods are isolated. We rotated the MTAB maps (g,j) so that the particle is vertical; experimental data is within the white boundaries. In (a−c), scale bars are 15 nm; in (d−i), scale bars are 10 nm.

the carbon signal on an absolute scale (see SI for further discussion). As described in the SI, we used each EELS map to calculate the binding density as a function of position by using a simple geometric model of the nanorod shape to map the



DOI: 10.1021/acs.nanolett.9b02434
Nano Lett. XXXX, XXX, XXX−XXX

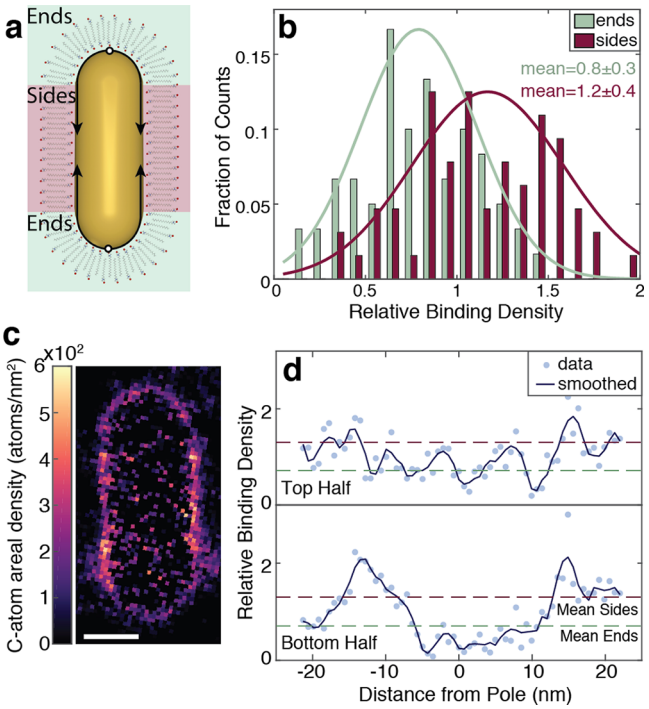


**Figure 3.** Quantification of the CTAB anisotropic distribution within a single AuNR. (a) Cartoon of CTAB on a AuNR (not to scale) showing designation of ends (green) and sides (red). (b) Histogram of the relative CTAB binding density (normalized to the mean) for the ends and sides of the nanorod along with Gaussian fits of the data to guide the eye. The fraction of counts for each curve is independently normalized. The mean binding density for the ends is 40% lower than for the sides. (c) EELS carbon compositional map of the CTAB-coated AuNR. Scale bar is 10 nm. (d) Line profile of the relative binding density as a function of distance along the AuNR surface of the particle from the poles (indicated by the white circles in (a)). Data is shown as points, displayed with a line smoothed using a Savitsky−Golay filter as a guide to the eye. We plot the path along the surface of the particle from left to right for both halves of the particle. We observe anisotropy in the ligand coating, with decreased relative binding density at the poles of the rod.

observed molecular distribution onto the nanorod surface. To obtain an estimate of the absolute value of the binding densities, we sum the total carbon intensity on each particle and divide by the surface area. Because damage from the electron beam can reduce the absolute carbon signals measured, these values represent a rough lower bound for the ligand density (see SI). Across all nanorods, we measure a mean binding density of 0.9 ± 0.2 (st. dev.) molecules/nm$^2$ for CTAB and 3.6 ± 1 (st. dev.) molecules/nm$^2$ for MTAB. These values are comparable to literature values, which range from 0.8 to 1.7 molecules/nm$^2$ for 0.1−10 mM CTAB on gold nanoparticles[37] and 3−5 molecules/nm$^2$ for MTAB-coated mini rods.[34]

Figure 3 illustrates these analyses applied to quantify the anisotropy of the CTAB coating for a single AuNR. First, we test whether binding density changes at the nanorod ends by sectioning the nanorod into areas of "ends" and "sides" as illustrated by the red/green coloring in Figure 3a. Figure 3b plots a histogram of binding densities for a single CTAB-coated nanorod, extracted from the EELS map in Figure 3c. Several attributes of the CTAB distribution are visible in these plots. First, CTAB binding density varies widely on a single nanorod, from a maximum of more than double the mean value to a minimum below our measurement sensitivity. These variations are higher than theoretical predictions of the facet-dependent variations in CTAB packing density, which vary by up to 12%.[7,8] Second, the distribution of binding densities at the ends of the nanorod has a lower mean and is narrower compared with the sides of the nanorod. The precise value of this decrease changes depending on where we place the boundary between "ends" and "sides" and reflects the average decrease across the entire "end" of the particle. Figure 3d shows line profiles of CTAB binding densities on the same particle; the origin is placed at the nanorod poles as indicated in Figure 3a. An interesting feature of Figure 3d is that it shows an anisotropic CTAB binding density that decreases near the ends of the nanorod. As shown in Figures S6 and S7, the overall distribution of CTAB does not change after EELS mapping for the acquisition conditions we used; a full discussion of the potential impact of electron beam damage on our results is available in the SI. To separate systematic trends in ligand coverage from random fluctuations, we repeated these analyses across multiple AuNRs with two different ligand types.

Figure 4 compares population-averaged ligand density measurements across 10 CTAB-coated AuNRs and 22 MTAB-coated mini AuNRs. MTAB-coated mini AuNRs offer a useful comparison with CTAB-coated nanorods. The two molecules are similar in length and structure (Figure 4a), but CTAB reportedly arranges in a bilayer[30,35] and MTAB thiol bonds in a self-assembled monolayer.[31] Indirect evidence from spatial reactivity of CTAB-coated nanorods[19−22] and $^1$H NMR measurements of the MTAB headgroup mobility[34] indicate that CTAB coatings decrease on the ends of the rods, while MTAB coatings are isotropic. By comparing the population-averaged CTAB data in Figures 4b,d to the individual nanorod data in Figure 3, we see that anisotropy in the ligand coverage is present in both data sets. The histograms in Figure 4b,c compare binding densities on the ends and sides of CTAB and MTAB ligands. The population-averaged data in Figure 4b echoes the behavior seen in Figure 3a for a single nanorod: again, we see that the normalized CTAB binding density decreases near the nanorod ends (0.88 ± 0.4 (st. dev.) at the ends and 1.03 ± 0.4 (st. dev.) at the sides). In contrast, the histogram of MTAB binding densities (Figure 4c) shows a more uniform distribution of binding densities across the particle (1.04 ± 0.2 (st. dev.) at the ends and 0.97 ± 0.2 (st. dev.) at the sides).

Figure 4d,e plot binding density profiles for all of the CTAB-coated AuNRs and MTAB-coated mini AuNRs. These plots condense the data from multiple nanorods into a single plot for each ligand type. Because the nanorods are nominally symmetric across their vertical and horizontal axes, we divide the data from each particle into four quarters. We plot all the unique data on the right half of the graph (positive position values) and mirror the data across $x = 0$ as a guide to the eye. Black lines indicate the median binding densities after smoothing. The CTAB coatings of AuNRs (Figure 4d) exhibit clear anisotropy: the ligand binding density decreases locally at the ends of the nanorod, reaching a minimum of around 70% of its mean value (0.68 ± 0.4 st. dev.) at the poles. In contrast, the MTAB-coated mini AuNRs (Figure 4e) indicate a more uniform ligand binding density along the nanorod, with a ∼10% increase across the ends of the particle. We also obtain excellent agreement between literature-reported chemical


DOI: 10.1021/acs.nanolett.9b02434
Nano Lett. XXXX, XXX, XXX−XXX

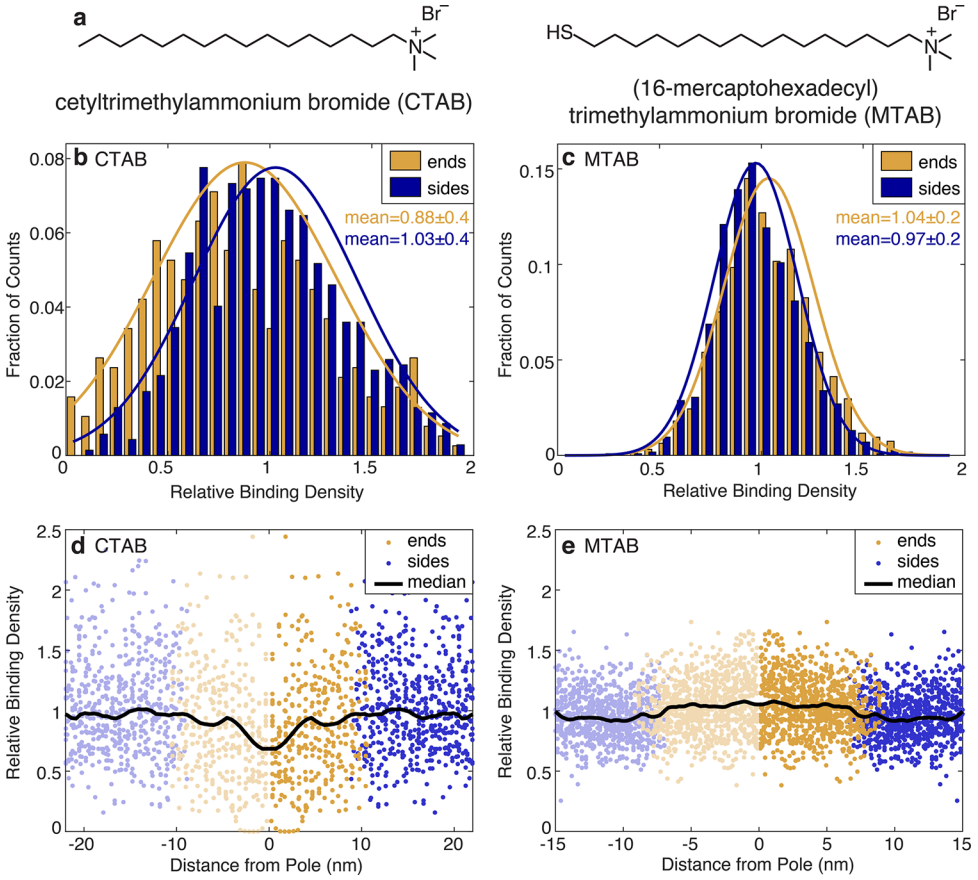


**Figure 4.** Quantification of the variation in CTAB and MTAB distributions between multiple AuNRs. (a) Structures of CTAB and MTAB. (b,c) Histograms of the relative binding densities (ends in yellow, sides in blue). To compare positional trends in binding density, binding densities are normalized to the mean of each nanorod. Because excess ligand may be trapped between adjacent particles where they are touching, we exclude these sections of particles from our analyses (see SI). (b) CTAB-coated data for 10 AuNRs. The mean value for the ends is 10% lower than for the sides. (c) Data for 22 MTAB-coated mini AuNRs where the mean value for the ends and the sides is the same within error. (d,e) Plots of the relative binding density as a function of position along the boundary, for (d) CTAB-coated AuNRs and (e) MTAB-coated mini AuNRs. The profiles in both (c) and (d) include data for individual rod quarters (scatter plot) and a Savitsky−Golay filtered median (black line plot). All unique data is plotted for positive $x$ values, and the plot is mirrored across $x = 0$ as a guide to the eye. The $x$-axes in (c) and (d) differ because the CTAB-coated AuNRs are larger than the MTAB-coated mini AuNRs. The profiles show anisotropy in the CTAB-coating with a decrease in the CTAB density approaching the poles, while the MTAB-coating shows a broad increase in MTAB density along the ends.

reactivities of the nanorods and the ligand distributions measured with EELS: CTAB-coated AuNRs exhibit higher reactivity at the ends of the nanorods,[19−22] where the lowest ligand densities are present. Overall, the population-averaged data show that we are able to clearly distinguish between the anisotropy of the distributions of CTAB[5,7,8] and MTAB[31,34] on AuNRs.

Our results demonstrate the application of EELS spectral imaging to directly image and quantify nanoscale anisotropies in the distribution of organic molecules on the surface of colloidal nanoparticles. While we focused on CTAB- and MTAB-coated AuNRs, these methods may be readily adapted to a broad range of nanomaterials and to study more complex phenomena such as variations in ligand distributions on different crystal facets. Our techniques open new avenues to visualize, measure, and understand heterogeneous and anisotropic molecular coatings and how they can be designed and harnessed to pattern functional properties on the nanoscale. These results bring us one step closer to controlling the formation of anisotropic structures and realizing a fundamental goal of materials science: rational synthesis of materials with tailored structure and shape.

## ■ ASSOCIATED CONTENT

### Supporting Information

The Supporting Information is available free of charge on the ACS Publications website at DOI: 10.1021/acs.nanolett.9b02434.

Nanoparticle synthesis and sample preparation, STEM imaging and EELS acquisition parameters, quantification of ligand binding density, and impact of electron beam damage (PDF)

## ■ AUTHOR INFORMATION

### Corresponding Author

*E-mail: pyhuang@illinois.edu.

### ORCID

Blanka E. Janicek: 0000-0002-5529-2819
Joshua G. Hinman: 0000-0002-1744-6661
Sang hyun Bae: 0000-0003-1625-7268
Meng Wu: 0000-0002-8533-6886
Jacob Turner: 0000-0001-6687-1536
Kenneth S. Suslick: 0000-0001-5422-0701



DOI: 10.1021/acs.nanolett.9b02434
Nano Lett. XXXX, XXX, XXX−XXX

Catherine J. Murphy: 0000-0001-7066-5575
Pinshane Y. Huang: 0000-0002-1095-1833

### Author Contributions

B.E.J. and P.Y.H. designed the experiment and performed the data analysis. B.E.J. and SH.B. performed electron microscopy under the supervision of P.Y.H. B.E.J., R.L., and E.P. performed graphene sample fabrication. J.G.H. and J.G.T. synthesized and characterized nanorod samples, both CTAB and silica-coated, under the supervision of C.J.M. M.W. and H.-H.C. developed the synthesis and characterized MTAB-coated mini nanorod samples under the supervision of C.J.M. J.J.H. and J.G.H. developed the ultrasonic nebulization deposition under the supervision of K.S.S. and C.J.M. J.J.H., J.G.H., J.G.T., H.-H.C., and M.W. performed the ultrasonic nebulization deposition. All authors contributed to the discussion of results and commented on and edited the paper. B.E.J. and P.Y.H. wrote the paper.

### Notes

The authors declare no competing financial interest.

## ■ ACKNOWLEDGMENTS

This work was supported by a Packard Foundation Fellowship and the National Science Foundation under award numbers DMR-1846206, CHE-1608743, CHE-1503408, and DMR-1720633. Electron microscopy was carried out in the University of Illinois at Urbana−Champaign Materials Research Laboratory Central Facilities and the Cornell Center for Materials Research Shared Facilities (DMR-1719875). The authors acknowledge useful discussions with Lena Fitting Kourkoutis. Electron microscopy support was provided by Malcolm Thomas, Jim Mabon, C. Q. Chen, and Wacek Swiech.

## ■ REFERENCES

(1) Watt, J.; Cheong, S.; Tilley, R. D. How to control the shape of metal nanostructures in organic solution phase synthesis for plasmonics and catalysis. *Nano Today* **2013**, *8* (2), 198−215.
(2) Yin, Y.; Alivisatos, a. P. Colloidal nanocrystal synthesis and the organic-inorganic interface. *Nature* **2005**, *437*, 664−670.
(3) Zhang, Z.; Glotzer, S. C. Self-Assembly of Patchy Particles. *Nano Lett.* **2004**, *4* (8), 1407−1413.
(4) Caswell, K. K.; Wilson, J. N.; Bunz, U. H. F.; Murphy, C. J. Preferential End-to-End Assembly of Gold Nanorods by Biotin−Streptavidin Connectors. *J. Am. Chem. Soc.* **2003**, *125* (46), 13914−13915.
(5) Burrows, N. D.; Vartanian, A. M.; Abadeer, N. S.; Grzincic, E. M.; Jacob, L. M.; Lin, W.; Li, J.; Dennison, J. M.; Hinman, J. G.; Murphy, C. J. Anisotropic Nanoparticles and Anisotropic Surface Chemistry. *J. Phys. Chem. Lett.* **2016**, *7*, 632−641.
(6) Nikoobakht, B.; El-Sayed, M. A. Preparation and Growth Mechanism of Gold Nanorods (NRs) Using Seed-Mediated Growth Method. *Chem. Mater.* **2003**, *15* (10), 1957−1962.
(7) Almora-Barrios, N.; Novell-Leruth, G.; Whiting, P.; Liz-Marzán, L. M.; López, N. Theoretical description of the role of halides, silver, and surfactants on the structure of gold nanorods. *Nano Lett.* **2014**, *14*, 871−875.
(8) Meena, S. K.; Sulpizi, M. Understanding the microscopic origin of gold nanoparticle anisotropic growth from molecular dynamics simulations. *Langmuir* **2013**, *29*, 14954−14961.
(9) Verma, A.; Uzun, O.; Hu, Y.; Hu, Y.; Han, H.-S.; Watson, N.; Chen, S.; Irvine, D. J.; Stellacci, F. Surface-structure-regulated cell-membrane penetration by monolayer-protected nanoparticles. *Nat. Mater.* **2008**, *7*, 588.
(10) Choueiri, R. M.; Galati, E.; Thérien-Aubin, H.; Klinkova, A.; Larin, E. M.; Querejeta-Fernández, A.; Han, L.; Xin, H. L.; Gang, O.; Zhulina, E. B.; Rubinstein, M.; Kumacheva, E. Surface patterning of nanoparticles with polymer patches. *Nature* **2016**, *538*, 79.
(11) Kim, J.-Y.; Han, M.-G.; Lien, M.-B.; Magonov, S.; Zhu, Y.; George, H.; Norris, T. B.; Kotov, N. A. Dipole-like electrostatic asymmetry of gold nanorods. *Science Advances* **2018**, *4* (2), e1700682.
(12) van Schooneveld, M. M.; Gloter, A.; Stephan, O.; Zagonel, L. F.; Koole, R.; Meijerink, A.; Mulder, W. J. M.; de Groot, F. M. F. Imaging and quantifying the morphology of an organic−inorganic nanoparticle at the sub-nanometre level. *Nat. Nanotechnol.* **2010**, *5*, 538.
(13) Koch, A. H. R.; Lévêque, G.; Harms, S.; Jaskiewicz, K.; Bernhardt, M.; Henkel, A.; Sönnichsen, C.; Landfester, K.; Fytas, G. Surface Asymmetry of Coated Spherical Nanoparticles. *Nano Lett.* **2014**, *14* (7), 4138−4144.
(14) Szekrényes, D. P.; Pothorszky, S.; Zámbó, D.; Osváth, Z.; Deák, A. Investigation of Patchiness on Tip-Selectively Surface-Modified Gold Nanorods. *J. Phys. Chem. C* **2018**, *122* (3), 1706−1710.
(15) Murphy, C. J.; Thompson, L. B.; Chernak, D. J.; Yang, J. A.; Sivapalan, S. T.; Boulos, S. P.; Huang, J.; Alkilany, A. M.; Sisco, P. N. Gold nanorod crystal growth: From seed-mediated synthesis to nanoscale sculpting. *Curr. Opin. Colloid Interface Sci.* **2011**, *16* (2), 128−134.
(16) Chang, H.-H.; Murphy, C. J. Mini Gold Nanorods with Tunable Plasmonic Peaks beyond 1000 nm. *Chem. Mater.* **2018**, *30* (4), 1427−1435.
(17) Lohse, S. E.; Murphy, C. J. Applications of Colloidal Inorganic Nanoparticles: From Medicine to Energy. *J. Am. Chem. Soc.* **2012**, *134* (38), 15607−15620.
(18) Lohse, S. E.; Murphy, C. J. The Quest for Shape Control: A History of Gold Nanorod Synthesis. *Chem. Mater.* **2013**, *25* (8), 1250−1261.
(19) Jana, N. R.; Gearheart, L.; Obare, S. O.; Murphy, C. J. Anisotropic Chemical Reactivity of Gold Spheroids and Nanorods. *Langmuir* **2002**, *18* (3), 922−927.
(20) Kou, X.; Sun, Z.; Yang, Z.; Chen, H.; Wang, J. Curvature-Directed Assembly of Gold Nanocubes, Nanobranches, and Nanospheres. *Langmuir* **2009**, *25* (3), 1692−1698.
(21) Wang, F.; Cheng, S.; Bao, Z.; Wang, J. Anisotropic overgrowth of metal heterostructures induced by a site-selective silica coating. *Angew. Chem., Int. Ed.* **2013**, *52*, 10344−10348.
(22) Hinman, J. G.; Eller, J. R.; Lin, W.; Li, J.; Li, J.; Murphy, C. J. Oxidation State of Capping Agent Affects Spatial Reactivity on Gold Nanorods. *J. Am. Chem. Soc.* **2017**, *139*, 9851−9854.
(23) González-Rubio, G.; Díaz-Núñez, P.; Rivera, A.; Prada, A.; Tardajos, G.; González-Izquierdo, J.; Bañares, L.; Llombart, P.; Macdowell, L. G.; Alcolea Palafox, M.; Liz-Marzán, L. M.; Peña-Rodríguez, O.; Guerrero-Martínez, A. Femtosecond laser reshaping yields gold nanorods with ultranarrow surface plasmon resonances. *Science* **2017**, *358* (6363), 640−644.
(24) Pérez-Juste, J.; Liz-Marzán, L. M.; Carnie, S.; Chan, D. Y. C.; Mulvaney, P. Electric-Field-Directed Growth of Gold Nanorods in Aqueous Surfactant Solutions. *Adv. Funct. Mater.* **2004**, *14* (6), 571−579.
(25) Lee, Z.; Jeon, K.-J.; Dato, A.; Erni, R.; Richardson, T. J.; Frenklach, M.; Radmilovic, V. Direct Imaging of Soft−Hard Interfaces Enabled by Graphene. *Nano Lett.* **2009**, *9*, 3365−3369.
(26) Algara-Siller, G.; Kurasch, S.; Sedighi, M.; Lehtinen, O.; Kaiser, U. The pristine atomic structure of MoS2 monolayer protected from electron radiation damage by graphene. *Appl. Phys. Lett.* **2013**, *103* (20), 203107.
(27) Hinman, J. G.; Hinman, J. J.; Janicek, B. E.; Huang, P. Y.; Suslick, K. S.; Murphy, C. J. Ultrasonic Nebulization for TEM Sample Preparation on Single-Layer Graphene Grids. *Nano Lett.* **2019**, *19*, 1938.
(28) Bang, J. H.; Suslick, K. S. Applications of Ultrasound to the Synthesis of Nanostructured Materials. *Adv. Mater.* **2010**, *22* (10), 1039−1059.


DOI: 10.1021/acs.nanolett.9b02434
*Nano Lett.* XXXX, XXX, XXX−XXX

(29) Hinman, J. J.; Suslick, K. S. Nanostructured Materials Synthesis Using Ultrasound. *Topics In Current Chemistry (Cham)* **2017**, *375* (1), 12.
(30) Nikoobakht, B.; El-Sayed, M. A. Evidence for Bilayer Assembly of Cationic Surfactants on the Surface of Gold Nanorods. *Langmuir* **2001**, *17* (20), 6368−6374.
(31) Vigderman, L.; Manna, P.; Zubarev, E. R. Quantitative Replacement of Cetyl Trimethylammonium Bromide by Cationic Thiol Ligands on the Surface of Gold Nanorods and Their Extremely Large Uptake by Cancer Cells. *Angew. Chem., Int. Ed.* **2012**, *51* (3), 636−641.
(32) Xin, H. L.; Mundy, J. A.; Liu, Z.; Cabezas, R.; Hovden, R.; Kourkoutis, L. F.; Zhang, J.; Subramanian, N. P.; Makharia, R.; Wagner, F. T.; Muller, D. A. Atomic-resolution spectroscopic imaging of ensembles of nanocatalyst particles across the life of a fuel cell. *Nano Lett.* **2012**, *12*, 490−497.
(33) Sau, T. K.; Murphy, C. J. Seeded High Yield Synthesis of Short Au Nanorods in Aqueous Solution. *Langmuir* **2004**, *20* (15), 6414−6420.
(34) Wu, M.; Vartanian, A. M.; Chong, G.; Pandiakumar, A. K.; Hamers, R. J.; Hernandez, R.; Murphy, C. J. Solution NMR Analysis of Ligand Environment in Quaternary Ammonium-Terminated Self-Assembled Monolayers on Gold Nanoparticles: The Effect of Surface Curvature and Ligand Structure. *J. Am. Chem. Soc.* **2019**, *141* (10), 4316−4327.
(35) Gómez-Graña, S.; Hubert, F.; Testard, F.; Guerrero-Martínez, A.; Grillo, I.; Liz-Marzán, L. M.; Spalla, O. Surfactant (Bi)Layers on Gold Nanorods. *Langmuir* **2012**, *28* (2), 1453−1459.
(36) Sau, T. K.; Murphy, C. J. Self-Assembly Patterns Formed upon Solvent Evaporation of Aqueous Cetyltrimethylammonium Bromide-Coated Gold Nanoparticles of Various Shapes. *Langmuir* **2005**, *21* (7), 2923−2929.
(37) Kawasaki, H.; Nishimura, K.; Arakawa, R. Influence of the Counterions of Cetyltrimetylammonium Salts on the Surfactant Adsorption onto Gold Surfaces and the Formation of Gold Nanoparticles. *J. Phys. Chem. C* **2007**, *111* (6), 2683−2690.


DOI: 10.1021/acs.nanolett.9b02434
*Nano Lett.* XXXX, XXX, XXX−XXX